Effect of Structural Symmetry on Magnetic, Electrical and Electrocatalytic Properties of Isoelectronic Oxides $A_2LaMn_2O_7$ ($A= Sr^{2+}, Ca^{2+}$)

Chandana C.W. Kananke-Gamage[a], Farshid Ramezanipour[a,]*

[a]Department of Chemistry, University of Louisville, Louisville, Kentucky 40292, USA
*Corresponding author. Email: farshid.ramezanipour@louisville.edu, Phone: +1(502) 852-7061
ORCID iD: 0000-0003-4176-1386

Abstract

The impact of structural symmetry on electrical charge transport, magnetism and electrocatalytic activity has been investigated in isoelectronic materials $Ca_2LaMn_2O_7$ and $Sr_2LaMn_2O_7$. These oxides form the so-called Ruddlesden-Popper structure, comprising bilayer stacks of MnO_6 octahedra, where Ca/Sr/La occupy the spaces within and between the stacks. The change in ionic radius from Ca^{2+} (1.18 Å) to Sr^{2+} (1.31 Å) results in a change in structural symmetry in these systems. $Ca_2LaMn_2O_7$ has an orthorhombic structure with *Cmcm* space group, whereas $Sr_2LaMn_2O_7$ features a tetragonal, *I4/mmm*, structure. The higher symmetry results in a significant variation of electrical, magnetic and electrocatalytic properties. $Sr_2LaMn_2O_7$ shows significantly greater charge transport in the entire temperature range of 25-800 °C, owing to a larger angle of Mn–O–Mn conduction pathway. In addition, the electrocatalytic properties of $Sr_2LaMn_2O_7$ for hydrogen-evolution reaction (HER) and oxygen-evolution reaction (OER) are enhanced as compared to $Ca_2LaMn_2O_7$. This is manifested in the improved overpotential for both HER and OER, as well as enhanced reaction kinetics. The improved OER/HER activity is also a function of structural features that produce greater electrical conductivity, which in turn affects the electrocatalytic properties.

Keywords: Symmetry, Structure, Electrical conductivity, OER, HER

Introduction

Ruddlesden-Popper (RP) oxides are a family of materials with general formula $A_{n-1}A'_2B_nO_{3n+1}$, where n = 1, 2, 3, ... represents the number of octahedral layers. The crystal structure of RP materials comprises A'_2O_2 layers alternating with stacks of BO_6 octahedra. The A-site is often occupied by a lanthanide, alkaline earth metal, or a mix of those, while the B-site usually contains a transition metal. The variation of A- and B-site metals in RP oxides can lead to changes in physical and chemical properties, such as crystal structure,[1-3] magnetism,[4-6] conductivity,[7-9] and electrochemical catalysis.[10, 11] For example, the impacts of having more than one type of A/A' cations and their ordering have been studied for manganese-based RP materials, where the stabilities and unit cell volumes are affected.[1] An increase in lattice parameters has been observed for $La_3Pr_1Ni_3O_{9.65}$ as compared to $La_2Pr_2Ni_3O_{9.65}$.[12] The former also shows higher power density when used as a cathode in intermediate temperature solid oxide fuel cells. [12]

Such effects have not been thoroughly studied in some other areas, such as their impact on electrocatalytic performance for water splitting. The electrochemical water-splitting has two half reactions, namely oxygen evolution reaction (OER) and the hydrogen evolution reaction (HER), both requiring an overpotential. However, the OER is known to be the bottleneck of water electrolysis due to the higher overpotential requirement.[13] The benchmark catalysts to overcome the sluggish kinetics of OER and HER are RuO_2, Ir-based catalysts and Pt, which are costly to use in large-scale applications. Therefore, there is considerable ongoing research on discovering economical catalysts for electrochemical water splitting, including various metal oxides.[14-17] Owing to their compositional diversity and the thermodynamic stability, multi-element transition metal oxides are promising candidates for electrocatalytic water splitting.[18-21] Our group has recently investigated a number of oxide materials for electrocatalytic water-splitting.[18-20, 22-25] In

particular, the relationship between crystal structure symmetry and electrocatalytic activity has been demonstrated. For example, the electrocatalytic activity of cubic $SrMnO_3$ has been shown to be significantly better than that of hexagonal $SrMnO_3$, highlighting the impact of crystal structure symmetry.[26] Another example is the structural change between $Sr_2Mn_2O_6$ and $CaSrMn_2O_6$, which are hexagonal $P6_3/mmc$ and cubic $Pm\text{-}3m$, respectively. The OER electrocatalytic activity of the latter material is significantly enhanced compared to the former.[27] In addition, it has been shown that in transition from $Sr_2FeCoO_{6-\delta}$ (disordered) to $CaSrFeCoO_{6-\delta}$ (ordered) and $Ca_2FeCoO_{6-\delta}$ (highly ordered), there is a systematic enhancement of the electrocatalytic activity.[28] Some Ruddlesden-Popper oxides have been studied for this purpose, where the change in the type of transition metal has been used to enhance the electrocatalytic activity. For example, an improved performance for both OER and HER electrocatalysis was observed for $Sr_2LaCoMnO_7$ as compared to $Sr_2LaFeMnO_7$.[29]

In the present study, we have investigated two isoelectronic Ruddlesden-Popper oxides, $Sr_2LaMn_2O_7$ and $Ca_2LaMn_2O_7$. Previous studies have reported magnetization and resistivity measurements for $Ca_2LaMn_2O_7$[30-32] and $Sr_2LaMn_2O_7$ at temperatures below 400 K.[5, 33, 34] The latter has also been studied for CO_2 conversion, oxygen reduction and electrochemical capacitance.[35, 36] However, their electrocatalytic properties for oxygen- and hydrogen-evolution reactions have not been studied. In this work, we have conducted a thorough investigation of electrocatalytic properties of $Sr_2LaMn_2O_7$ and $Ca_2LaMn_2O_7$ toward both components of water splitting, namely OER and HER. We have demonstrated the effect of the structural symmetry on electrocatalytic properties in these isoelectronic materials. We have also shown that these changes are associated with the improvement of electrical charge transport in a wide range of temperatures from 25 °C to 800 °C.

2. Experimental

2.1 Synthesis

$Sr_2LaMn_2O_7$ and $Ca_2LaMn_2O_7$ were prepared by solid-state synthesis method using powders of $CaCO_3$, $SrCO_3$, La_2O_3, MnO_2, Fe_2O_3 and CoO. The stoichiometric amounts of oxides/carbonates were mixed thoroughly using agate mortar and pestle. The mixtures were pressed into pellets and heated at 1300 °C in air for 24 hours. The samples were then re-ground and re-pelletized to be heated at 1300 °C for a total of 72 hours in air with two intermittent grindings and pelletizing. The heating and cooling rates of the furnace for all samples were 100 °C/hour.

2.2 Characterization

The synthesized materials were characterized using a high-resolution X-ray diffractometer with Cu Kα1 (λ = 1.54056 Å). The data were collected in the 2θ range of 10 - 80°. Rietveld refinements for the X-ray diffraction (XRD) data were carried out using GSAS software[37] and the EXPGUI interface.[38] The electrical conductivity measurements were conducted by two-probe direct current method using an applied potential of 0.01 V. Magnetic susceptibility data were obtained in the temperature range of 2 to 400 K with an applied magnetic field of 1000 Oe on a vibrating sample magnetometer. For each material, data were obtained by lowering the temperature without the external magnetic field (zero field cooled: ZFC) and with the external field (field cooled: FC). Isothermal field-run measurements were also performed in magnetic fields of 0 – 9 T. Iodometric titrations[39] were performed to examine the oxygen stoichiometries of the two materials. 50 mg of the sample and excess KI (2 g) were dissolved in 100 ml of 1 M HCl, and the mixture was left to react overnight. Then 5 ml of the mixture was pipetted out and the iodine that had been generated was titrated against 0.025 M $Na_2S_2O_3$. All steps of the titration were performed under argon

atmosphere. A volume of 0.6 ml (12 drops) of a starch solution was used as indicator near the endpoint of the titration. Calculations are based on the conversion of transition metal ions (Mn^{3+} and Mn^{4+}) into Mn^{2+} due to the excess KI. The consumed moles of titrant ($Na_2S_2O_3$) to titrate 5 ml of the titrand were determined based on the concentration and titration volume of $Na_2S_2O_3$. The amount of oxygen that was lost due to the reduction of the metals is equivalent to the amount of I_2 that is titrated by $Na_2S_2O_3$. The total amount of oxygen is therefore the sum of the remaining oxygen (to balance the charge of Mn^{2+}) and the lost oxygen (due to reduction of Mn^{3+} and Mn^{4+} into Mn^{2+}).

2.3 Electrochemical OER/HER studies

The catalyst ink of each material was prepared by mixing 35 mg of the powder sample, 7 mg of carbon black powder (Fuel Cell Store), 40 µL Nafion® D-521 solution (Alfa Aesar, 5% w/w in water and 1-propanol), and 7 ml of tetrahydrofuran (Alfa Aesar, 99%). The mixture was then sonicated for 30 minutes. A glassy carbon electrode (GCE, 5 mm diameter, 0.196 cm^2 area, HTW Germany) was used as the working electrode. Prior to use, it was cleaned using aluminum oxide polishing solution (Allied Hightech Products Inc.) on a polishing cloth, followed by sonication for 2-3 minutes in ethanol (Decon Labs, Inc.). At the end of the polishing steps, the GCE was washed with deionized water and dried. Then 20 µl of the prepared catalyst ink was drop-casted on the surface of the GCE by placing two coats of 10 µl with a 2-minute interval. Total catalyst mass loading on the GCE was 0.1 mg. The GCE was then left overnight to air-dry before running the OER/HER electrochemical measurements.

The electrochemical OER/HER experiments were carried out on a standard three-electrode cell using an electrode rotator at 1600 rpm. Commercial Ag/AgCl electrode in 1 M KCl (CH

instruments, Inc., TX, USA) and 4 M KCl (Pine Research instruments) were utilized as reference electrodes for OER and HER experiments, respectively. A platinum electrode (Pine Research Instruments) and a carbon electrode were used as counter electrodes for the OER and HER measurements, respectively. Chronopotentiometry experiments in acidic conditions for HER were done by loading a total of 20 µl catalyst ink on the GCE using two coats of 10 µl with a 2-minute interval, followed by overnight air-drying. Carbon electrode was used as counter electrode in a three-electrode setup. Voltage was collected for 10 hours, while applying a constant current of -1.9 mA (~ -10 mA/cm^2). Chronopotentiometry experiments in alkaline conditions were done on two-electrode cells using nickel foam, with applied currents of 2 mA and -10 mA, for OER (0.1 M KOH) and HER (1 M KOH), respectively. For OER, 2 mA was chosen due to the low current observed in the polarization curves. Each electrode consisted of 1 cm^2 nickel foam, on which 100 µl of the catalyst ink had been dropcasted with 20 µl increments, followed by overnight air-drying. The two electrodes, which had been separated by two layers of glass fiber filter paper, were attached to gold wires, which were then connected to the potentiostat. Prior to conducting the chronopotentiometry experiment, the two electrodes were soaked in the electrolyte for at least 12 hours. The potential versus Ag/AgCl electrode ($E_{Ag/AgCl}$) was converted to be expressed against RHE using the equation $E_{RHE} = E_{Ag/AgCl} + 0.059\ pH + E^{o}_{Ag/AgCl}$, where $E^{o}_{Ag/AgCl} = 0.21$ V for 3M KCl[40] and 0.197 V for 4 M KCl.[41, 42]

3. RESULTS AND DISCUSSION

3.1 Crystal Structure

Rietveld refined profiles for $Sr_2LaMn_2O_7$ and $Ca_2LaMn_2O_7$ are shown in Figure 1 and their refined structural parameters are reported in Tables 1 and 2.

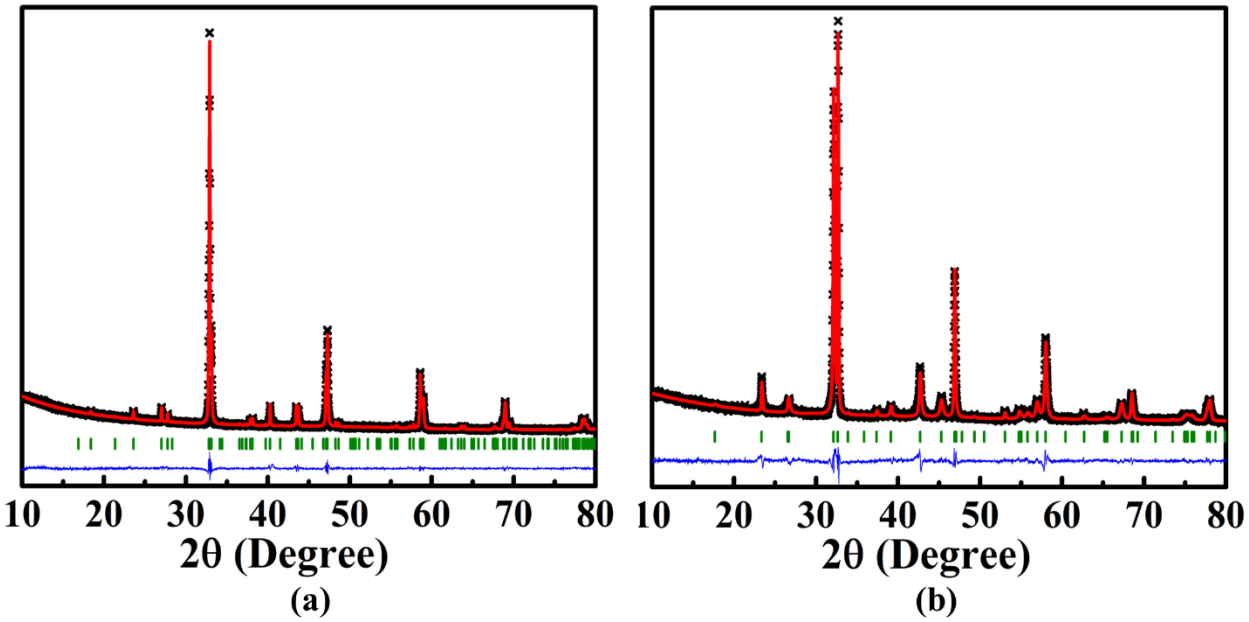

Figure 1. Rietveld refinement profiles for powder X-ray diffraction data for (a) $Ca_2LaMn_2O_7$ and (b) $Sr_2LaMn_2O_7$. The experimental data are represented by black crosses. The red line shows the fit. The vertical green tick marks and the lower blue line correspond to the Bragg peak positions and difference plot, respectively.

Table 1. Refined structural parameters of $Ca_2LaMn_2O_7$ from powder X-ray diffraction data. Space group: *Cmcm*, a = 19.2814(4) Å, b = 5.4609(1) Å, c = 5.4113(1) Å, Rp = 0.0261, wRp = 0.0341

Atom	x	y	z	Occupancy	U_{iso} (Å^2)	Multiplicity
Ca1	0	0.248(2)	0.25	0.37(1)	0.028(3)	4
La1	0	0.248(2)	0.25	0.63(1)	0.028(3)	4
Ca2	0.1886(2)	0.242(2)	0.25	0.782(7)	0.052(3)	8
La2	0.1886(2)	0.242(2)	0.25	0.218(7)	0.052(3)	8
Mn	0.3995(3)	0.247(3)	0.25	1	0.017(3)	8
O1	0	0.683(8)	0.25	1	0.037(4)	4
O2	0.300(1)	0.290(5)	0.25	1	0.037(4)	8
O3	0.096(1)	0	0	1	0.037(4)	8
O4	0.393(1)	0	0	1	0.037(4)	8

Table 2. Refined structural parameters of $Sr_2LaMn_2O_7$ from powder X-ray diffraction data. Space group: *I4/mmm*, $a = b = 3.8670(1)$ Å, $c = 19.9814(10)$ Å, Rp = 0.0415, wRp = 0.0549

Atom	x	y	z	Occupancy	U_{iso} (Å^2)	Multiplicity
Sr1	0	0	0.5	0.60(3)	0.037(2)	2
La1	0	0	0.5	0.40(3)	0.037(2)	2
Sr2	0	0	0.3153(1)	0.73(3)	0.041(2)	4
La2	0	0	0.3153(1)	0.27(3)	0.041(2)	4
Mn	0	0	0.1007(4)	1	0.021(2)	4
O1	0	0	0	1	0.098(4)	2
O2	0	0	0.199(1)	1	0.098(4)	4
O3	0	0.5	0.095(1)	1	0.098(4)	8

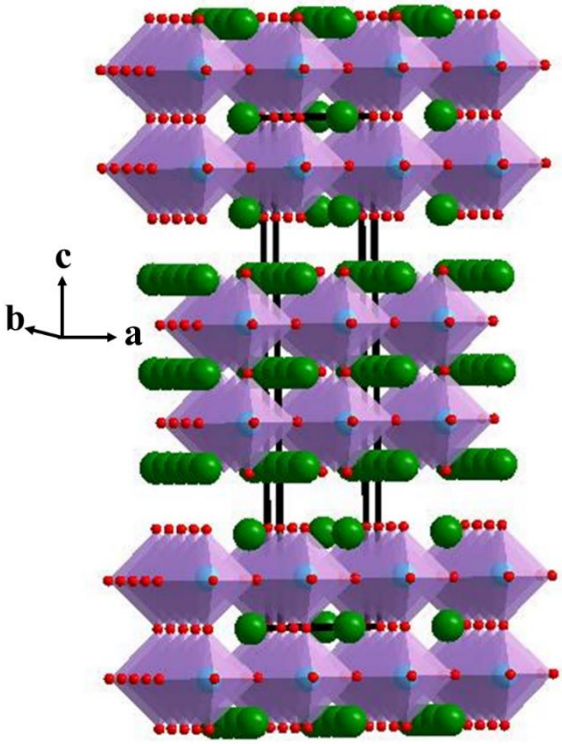

Figure 2. Crystal structure of $A_2LaMn_2O_7$ (A=Ca/Sr). Green spheres represent Ca/Sr/La and red spheres are oxygen. The Mn atoms are shown as light blue spheres at the centers of MnO_6 octahedra.

As shown in Figure 2, the crystal structures of these Ruddlesden-Popper type oxides comprise bilayer stacks of MnO_6 octahedra, which are connected via corner-sharing. For each MnO_6 octahedron, one apical oxygen atom and four equatorial oxygens are involved in forming the

bilayer stack. Each MnO_6 octahedron has one apical oxygen which is not shared with other octahedra. The La/Ca/Sr atoms are located in spaces between and within the bi-layer stacks. The difference in the ionic radii of Ca^{2+} (1.18 Å) and Sr^{2+} (1.31 Å for CN = 9)[43] results in a change in structural symmetry of these isoelectronic materials. $Ca_2LaMn_2O_7$[44] crystallizes in the orthorhombic *Cmcm* space group, while $Sr_2LaMn_2O_7$ [33] has a tetragonal *I*4/*mmm* space group, consistent with previous reports.[44,33] The tilting and fine rotations of MnO_6 octahedra in $Ca_2LaMn_2O_7$, caused by the smaller ionic radius of Ca^{2+}, result in anisotropic Mn-O bond distances with four types of oxygens as shown in Table 3.

Table 3. Mn-O bond distances and Mn-O-Mn angles or $Sr_2LaMn_2O_7$ and $Ca_2LaMn_2O_7$

$Sr_2LaMn_2O_7$	
Mn–O1	2.012(8)
Mn–O2	1.965(23)
Mn–O3 × 4	1.9366(13)
Average Mn–O	1.9539(15)
Mn–O1–Mn	180.0(0)
Mn–O3–Mn	173.5(13)
Average Mn-O-Mn	176.75(9)
$Ca_2LaMn_2O_7$	
Mn–O1	1.970(11)
Mn–O2	1.924(23)
Mn–O3 × 2	1.936(12)
Mn–O4 × 2	1.915(12)
Average Mn–O	1.9326(14)
Mn–O1–Mn	159.4(25)
Mn–O3–Mn	174.4(16)
Mn–O4–Mn	172.4(15)
Average Mn–O–Mn	168.73(19)

The average Mn-O bond length for $Ca_2LaMn_2O_7$ is shorter than that of $Sr_2LaMn_2O_7$ (Table 3), consistent with the effect of the ionic radius in expanding the lattice of the latter material. The normalized unit cell volume for $Ca_2LaMn_2O_7$, 284.89 $Å^3$ (normalized by dividing the tetragonal unit cell volume, 569.78 $Å^3$, by 2), is smaller than that of $Sr_2LaMn_2O_7$, 298.79 $Å^3$. The microstructures of the two materials were evaluated using scanning electron microscopy, as shown in Figure 3. As seen here, $Sr_2LaMn_2O_7$ has smaller grains compared to $Ca_2LaMn_2O_7$. The oxygen contents were confirmed using iodometric titrations, indicating 7 oxygens per unit formula unit for both materials.

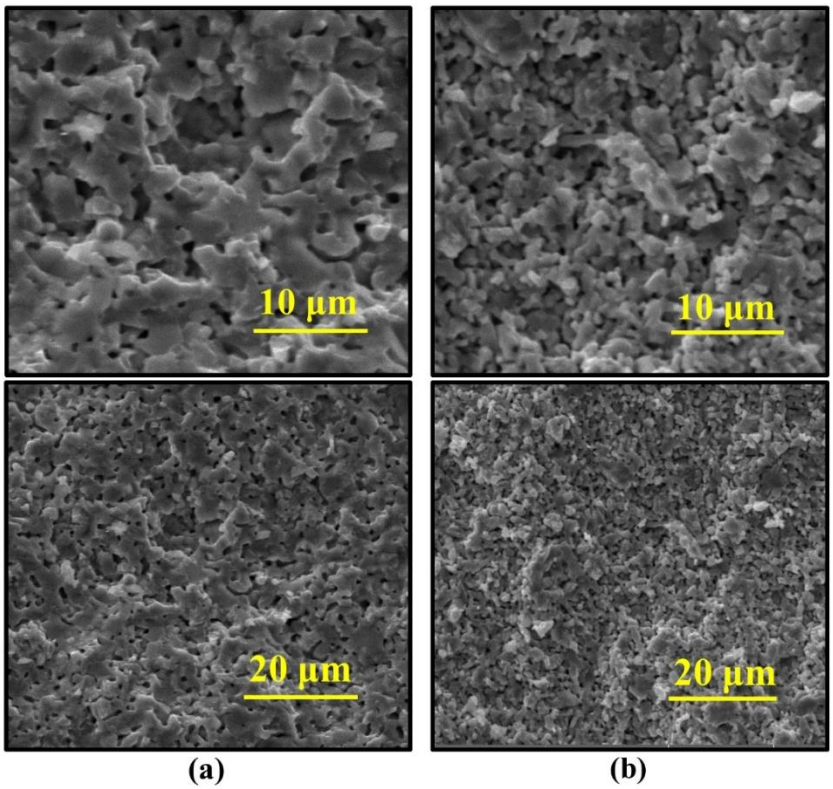

Figure 3. Scanning electron microscopy images of (a) $Ca_2LaMn_2O_7$ and (b) $Sr_2LaMn_2O_7$.

3.2 Electrical Conductivity

The electrical properties of these materials were investigated in the temperature range 25-800 ºC. The following equation was used to calculate conductivities using the measured resistance (R) values at a given constant voltage.[45]

$$\sigma = L/RA \quad (1)$$

In the above equation, σ is the conductivity, L is the thickness of the cylindrical pellet, and A is the cross-sectional area calculated using $A= \pi r^2$, where r is the radius of the pellet. The electrical conductivity variation as a function of temperature is illustrated in Figure 4a. The conductivity of both materials increases as a function of temperature up to 400 ºC for $Sr_2LaMn_2O_7$ and 500 ºC for $Ca_2LaMn_2O_7$, which is a typical behavior of semiconductors. However, beyond those temperatures, a transition occurs where the electrical conductivity decreases as a function of temperature, which is a characteristic metallic behavior. $Sr_2LaMn_2O_7$ shows higher conductivity than $Ca_2LaMn_2O_7$ through the entire temperature range, indicating the impact of structural properties on conductivity. Generally, the hetero-valency of the B-site cation is important for electrical conduction in oxides. In Ruddlesden-Popper oxides, the B-site cations are usually transition metals. The overlap of the 3d orbitals of transition metals with the 2p orbitals of oxygen facilitates the conduction via B-O-B pathways using electrons or holes. Greater metal overlap between these orbitals can be achieved by shorter B-O bonds and larger B-O-B angles to enhance the electrical conductivity.[46] In the case of materials studied in this work, the type of transition metal is the same in both compounds. Therefore, the effects of structural distortions and bond angles becomes prominent. The average Mn-O-Mn bond angles in $Sr_2LaMn_2O_7$ is closer to 180° degrees (Table 3), hence providing an improved orbital overlap and enhanced conduction through the Mn-O-Mn pathway. This is a consequence of the more symmetrical structure of $Sr_2LaMn_2O_7$

(tetragonal) as opposed to that of $Ca_2LaMn_2O_7$ (orthorhombic), which contains more distortions due to the smaller ionic radius of calcium.

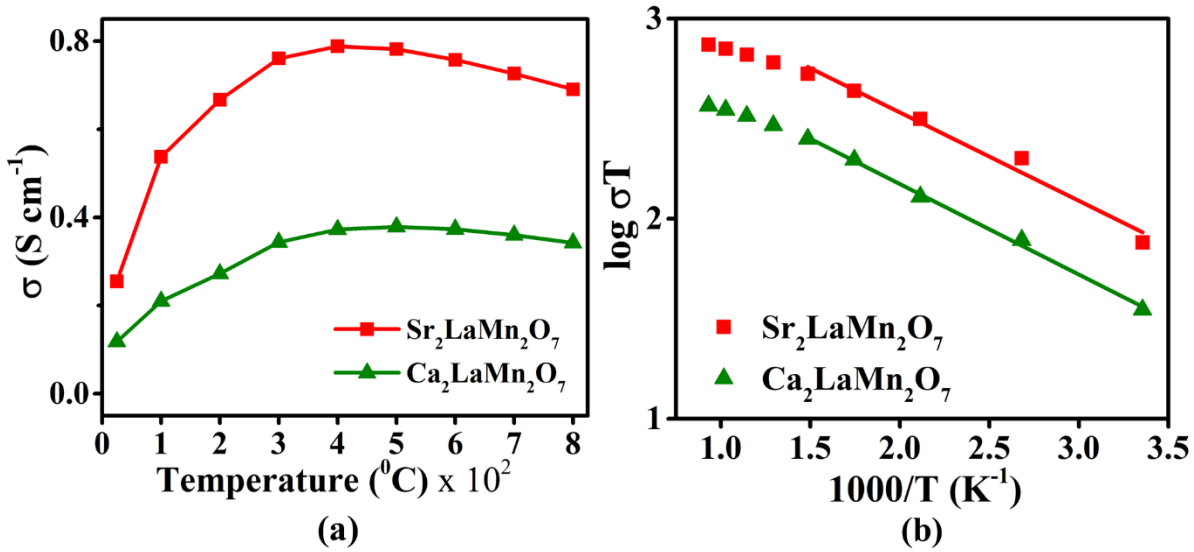

Figure 4. (a) Electrical conductivity variation as a function of temperature. (b) Arrhenius plots for determination of the activation energies (E_a) for the temperature-activated increase in conductivity, giving E_a = 0.0877 (25-500 °C) for $Sr_2LaMn_2O_7$ and E_a = 0.0898 (25-400 °C) for $Ca_2LaMn_2O_7$.

The activation energy associated with the thermally activated increase in conductivity[47] can be calculated using the Arrhenius equation shown below, where σ, σ_0, T, E_a, and K_B represent the conductivity, pre-exponential factor, temperature, activation energy, and Boltzmann constant, respectively.

$$\sigma T = \sigma_0 e^{-\frac{E_a}{2.303\,K_B T}} \qquad (2)$$

The Arrhenius plots for the two materials are shown in Figure 4b. The activation energies calculated using the Arrhenius plots (log σT vs 1000/T) show similar activation energies for both compounds in the range 25 – 400 °C. This indicates that the rate of increase in electrical conductivity as a function of temperature is similar in the two materials.

3.3 Magnetic Properties

Structural changes also have a notable impact on magnetic properties. Magnetic susceptibility (χ) measurements were carried out in the temperature range 2 K – 400 K. As shown in Figure 5a, there is a sharp increase in susceptibility for $Ca_2LaMn_2O_7$, as the temperature is lowered below ~280 K, indicative of ferromagnetic interactions, similar to the behavior observed in a previous study.[44] The isothermal magnetization versus field data at 300 K shows a linear increase as a function of field, a typical paramagnetic behavior. However, the isothermal magnetization at 5 K shows a sharp increase at low field, but saturation is not reached up to 9 T. A small hysteresis is also present in the isothermal magnetization data at 5 K, consistent with a weak ferromagnetic behavior.

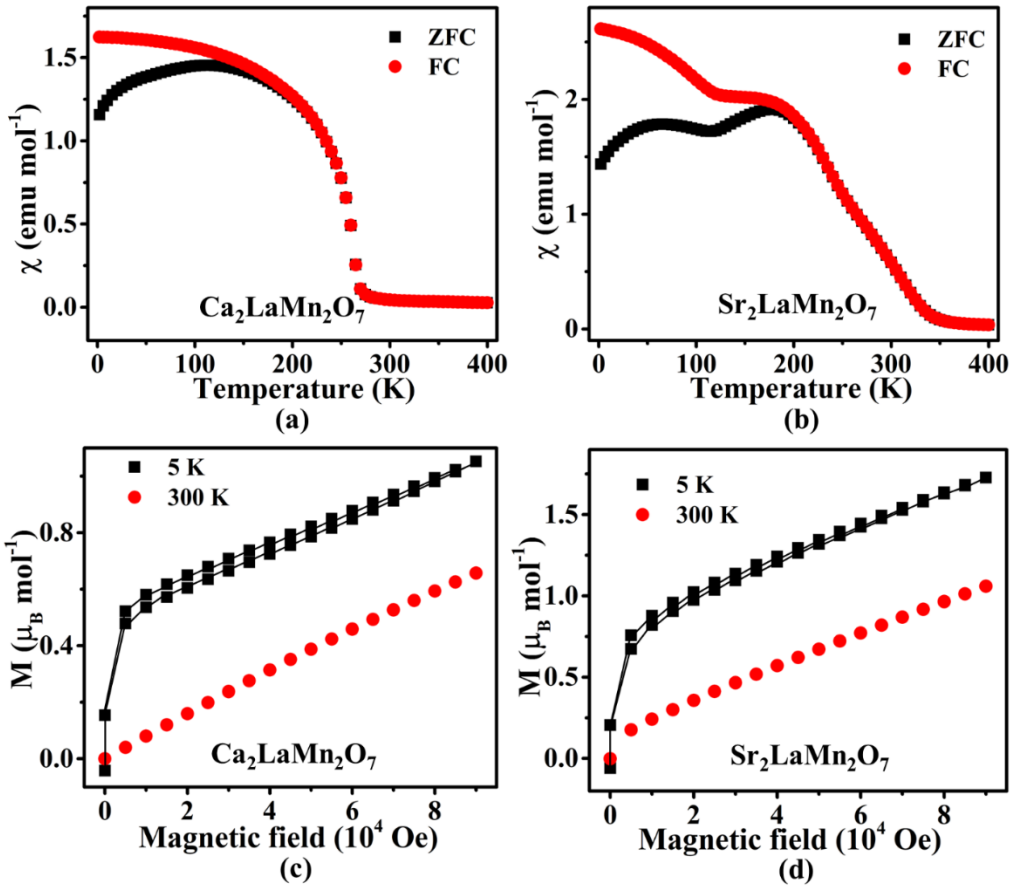

Figure 5. (a) and (b) show zero-field-cooled (ZFC) and field-cooled (FC) magnetic susceptibility data. (c) and (d) show the isothermal magnetization data as a function of magnetic field. The lines are guide to the eye.

The magnetic susceptibility and isothermal field sweep data for $Sr_2LaMn_2O_7$ show a different behavior. As demonstrated in Figure 5b, the data for $Sr_2LaMn_2O_7$ shows a rise in the susceptibility value below 350 K. Further decrease in temperature leads to a transition below ~220 K. The isothermal magnetization versus field data at 5 K show an initial sharp increase in magnetization, followed by a more modest rise as a function of the field, without reaching saturation in the range of 0 – 9 T. Taken together, the variable temperature susceptibility and isothermal magnetization data indicate competing ferro- and antiferromagnetic behaviors for $Sr_2LaMn_2O_7$, consistent with a previous report.[48] The isothermal magnetization at 300 K shows a sharp increase up to ~0.5 T, followed by a linear rise with a smaller slope at higher fields. This confirms that ferromagnetic interactions are present at room temperature as well.

3.4 Electrocatalytic Properties for OER and HER

An important impact of the change in the structure is observed in the electrocatalytic properties toward both half reactions of water-splitting, i.e., oxygen evolution reaction (OER) and hydrogen evolution reaction (HER). The electrocatalytic activities for OER in 0.1 M KOH are shown in Figure 6. Measurements in other conditions, such as 1M KOH and 0.1 M $HClO_4$, led to rapid deterioration of the current response. While both materials show low activity and a low current, the effect of structural change is clear. $Sr_2LaMn_2O_7$, which has a higher symmetry, shows better performance, evident from lower onset potential, where the electrocatalytic reaction begins and the polarization curve deviates from a horizontal line to show an increase in current response. In addition, the current generated using $Sr_2LaMn_2O_7$ at the same potential is greater than that of $Ca_2LaMn_2O_7$. Furthermore, $Sr_2LaMn_2O_7$ shows better reaction kinetics, evaluated using the Tafel equation $\eta = a + b\ logj$, where η is the overpotential and j is the current density.[18, 47] The slope

of the plot of η versus log j, i.e., Tafel slope (Figure 6b), is indicative of the reaction kinetics and is affected by electron and mass transport. In general, lower Tafel slopes show better kinetics of the OER reaction. As shown in Figure 6b, the Tafel slope for $Sr_2LaMn_2O_7$ is smaller than that of $Ca_2LaMn_2O_7$, consistent with better kinetics and higher electrocatalytic activity of the former material.

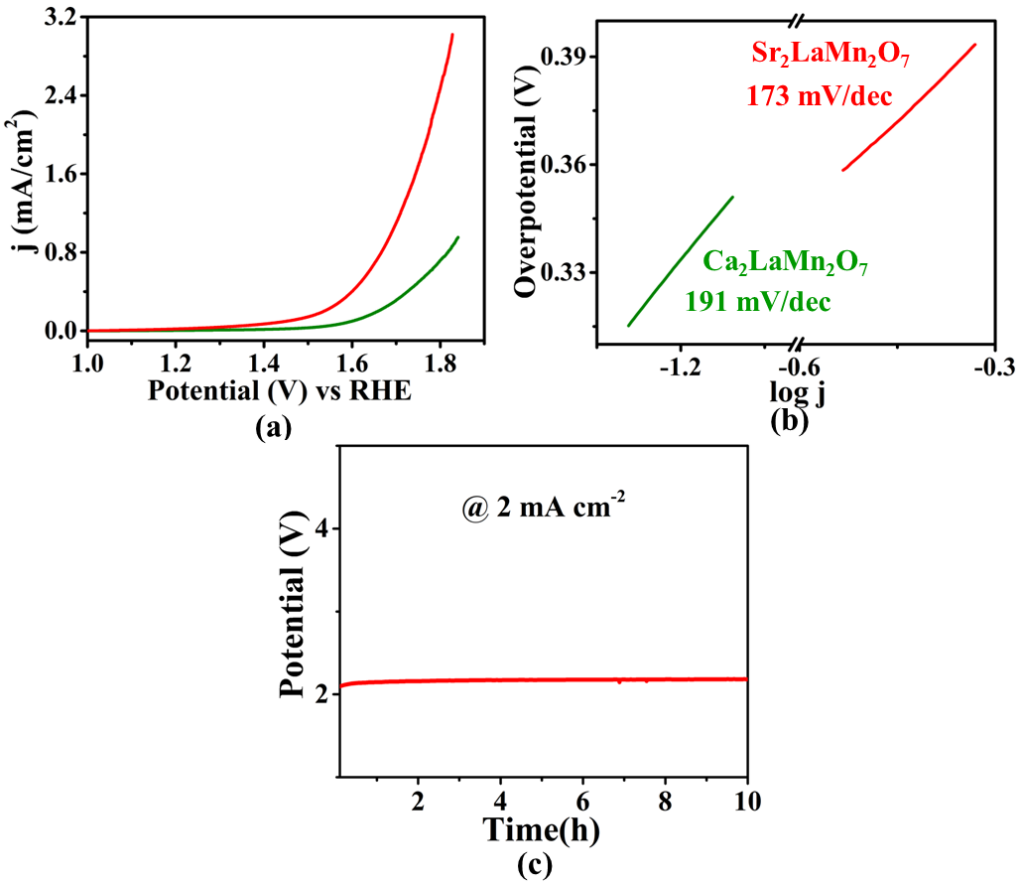

Figure 6. OER activity in 0.1 M KOH for $Sr_2LaMn_2O_7$ (red) and $Ca_2LaMn_2O_7$ (green): **(a)** Polarization curves, **(b)** Tafel plots and **(c)** Chronopotentiometry response of $Sr_2LaMn_2O_7$.

The electrocatalytic properties for HER show a greater current response, especially in acidic condition, 0.5 M H_2SO_4. Figure 7a shows the polarization curves of the two materials, where $Sr_2LaMn_2O_7$ gives a lower onset potential than $Ca_2LaMn_2O_7$. In addition, the overpotential at 10 mA/cm^2 (η_{10}) is commonly used as a reference for comparing different electrocatalysts. Again,

$Sr_2LaMn_2O_7$ (η_{10} = 0.589 V) shows a lower overpotential than $Ca_2LaMn_2O_7$ (η_{10} = 0.595 V). Although the performance of these materials is not as high as Pt/C[49, 50] (shown in black in Figure 7a) or some other oxide catalysts such as $CaSrFe_{0.75}Co_{0.75}Mn_{0.5}O_{6-\delta}$,[22] they show a better performance than some reported HER electrocatalysts such as WO_3 (η_{10} = 0.637 V)[51] and TiO_{2-x} (η_{10} = 0.630 V).[52]

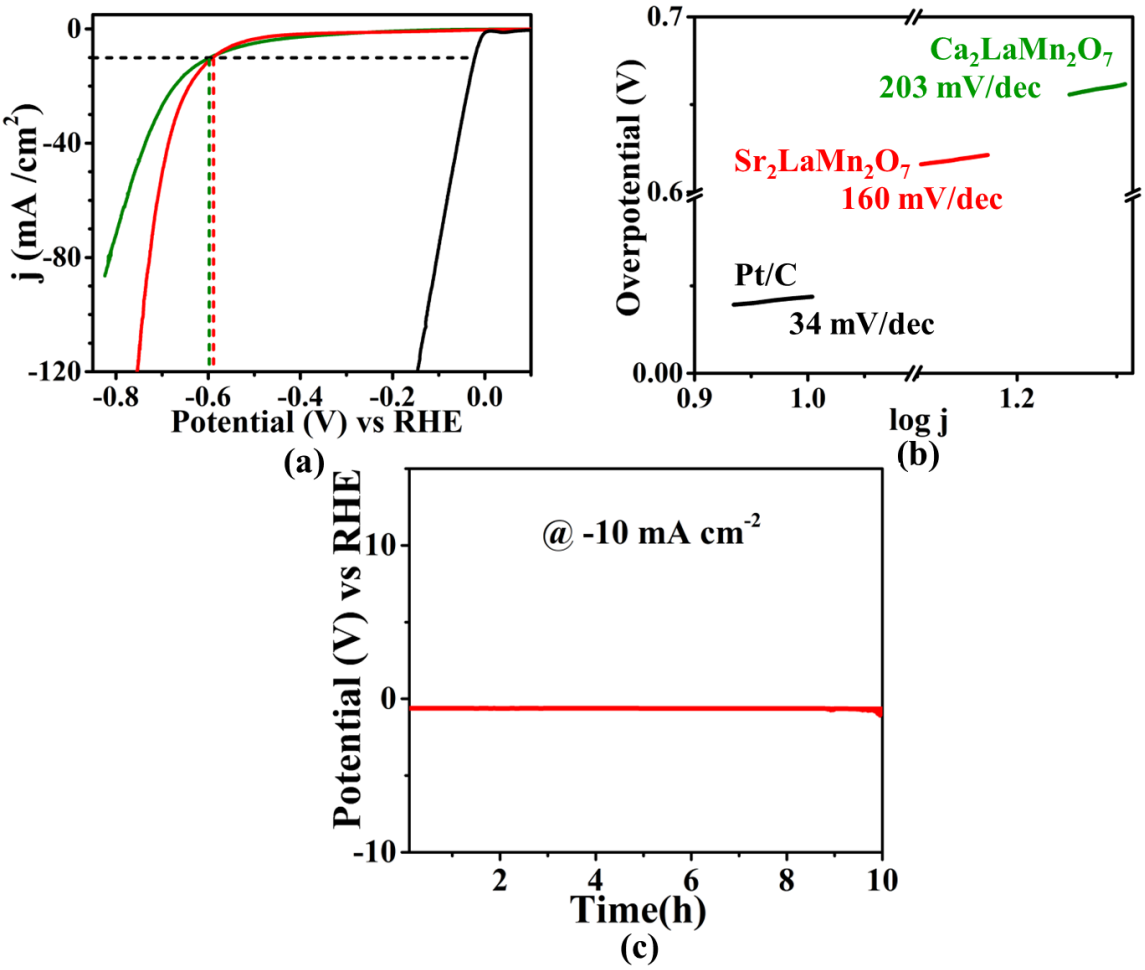

Figure 7. (a) HER polarization curves in 0.5 M H_2SO_4 for $Ca_2LaMn_2O_7$ (green) and $Sr_2LaMn_2O_7$ (red). (b) Tafel plots and Tafel slopes. (c) Chronopotentiometry data for $Sr_2LaMn_2O_7$.

Figure 7b shows the Tafel plots for HER, where $Sr_2LaMn_2O_7$ has a smaller Tafel slope than $Ca_2LaMn_2O_7$, indicating faster reaction kinetics for the former material. This is in line with the

higher HER activity of $Sr_2LaMn_2O_7$, which also shows a sustained response for at least 10 hours, as demonstrated by chronopotentiometry data in Figure 7c.

HER experiments were also done in alkaline conditions, as shown in Figures S7 and S8, indicating higher overpotentials. However, the catalysts have better stability in alkaline conditions. Even though the catalysts are able to catalyze the HER in acidic condition, we have found the catalytic material is partially decomposed under those conditions. However, at least some portion of the catalyst remains intact to give a stable current response for 10 hours in chronopotentiometry experiments. As demonstrated by X-ray diffraction experiments before and after 500 cycles, the main peaks corresponding to our catalyst are still present after 500 cycles, but there is evidence of gradual decomposition of the material in acidic conditions, indicated by the appearance of new peaks (Figure S2). On the other hand, in alkaline conditions, X-ray diffraction experiments before and after 500 cycles show that the material remains intact and retains its structural integrity, with no new peaks appearing in the diffraction data after 500 cycles (Figure S3).

The double layer capacitance values, C_{dl},[53] were also obtained for both materials using cyclic voltammetry in the non-Faradaic region (Figures S5a and b), where the current stems from electrical double layer charge and discharge. The average of j_{anodic} and $j_{cathodic}$ at the middle potential of the cyclic voltammetry data ($j_{average}$) is plotted against the scan rate ν based on the equation $C_{dl} = j_{average}/\nu$. Therefore, the C_{dl} value is obtained from the slope of the $j_{average}$ vs ν plot.[22, 54] As shown in Figure S5, the C_{dl} value for $Sr_2LaMn_2O_7$ is greater than that of $Ca_2LaMn_2O_7$. The importance of C_{dl} is that it is proportional to the electrochemically active surface area.[19, 23, 55]

The enhanced electrocatalytic activity of $Sr_2LaMn_2O_7$ may be understood in the context of its structural features. The HER process involves the adsorption of hydrogen atoms on the catalyst surface as intermediate species before forming hydrogen molecules.[56] Various descriptors have

been proposed to explain the HER activities of different catalysts. Among them, some are related to structural features, where the HER performance is correlated with the bond length between the transition metal and the non-metal anion.[10, 57] Some researchers have proposed that longer distances between the metal and non-metal sites allow for greater electron localization on the non-metal site, favoring the adsorption of hydrogen and final transformation into hydrogen molecules.[57] As shown in Table 3, the average Mn-O bond length for $Sr_2LaMn_2O_7$ is greater than that of $Ca_2LaMn_2O_7$, which is consistent with the above descriptor, relating the HER activity to bond length. In addition, the average Mn–O–Mn bond angle for $Sr_2LaMn_2O_7$ is larger, leading to a better alignment of metal d and oxygen p orbitals and higher electrical conductivity. Given that HER is an electron transfer process, the enhanced electrical charge transport of $Sr_2LaMn_2O_7$ can also contribute to its greater electrocatalytic performance.

Conclusions

The structural symmetry has an important impact on electrical charge transport, magnetism and electrocatalytic activity, as demonstrated for isoelectronic oxides $Ca_2LaMn_2O_7$ and $Sr_2LaMn_2O_7$. The higher symmetry of the latter leads to enhanced electrical conductivity and greater electrocatalytic performance for both half-reactions of water-splitting, i.e., HER and OER. $Sr_2LaMn_2O_7$ shows lower onset and overpotentials for these electrocatalytic processes, as well as better reaction kinetics. The improved activity of this material may be related to longer bond distances, which are proposed to correlate with electrocatalytic performance. In addition, greater bond angles lead to enhanced electrical conductivity, which in turn can have a positive impact on electrocatalytic properties, which involve the transfer of electrons.

Acknowledgement. This work is supported by the National Science Foundation (NSF) under grant no. DMR-1943085.

References

(1) Fanah, S. J.; Ramezanipour, F. Lithium-ion mobility in layered oxides $Li_2Ca_{1.5}Nb_3O_{10}$, $Li_2Ca_{1.5}TaNb_2O_{10}$ and $Li_2Ca_{1.5}Ta_2NbO_{10}$, enhanced by supercell formation. *J. Energy Chem.* **2021**, *60*, 75-84.

(2) Fanah, S. J.; Ramezanipour, F. Symmetry Effect on the Enhancement of Lithium-Ion Mobility in Layered Oxides $Li_2A_2B_2TiO_{10}$ (A = La, Sr, Ca; B = Ti, Ta). *J. Phys. Chem. C* **2021**, *125* (7), 3689-3697.

(3) Fanah, S. J.; Yu, M.; Huq, A.; Ramezanipour, F. Insight into lithium-ion mobility in $Li_2La(TaTi)O_7$. *J. Mater. Chem. A* . **2018**, *6* (44), 22152-22160.

(4) Lun-hua, H.; Pan-lin, Z.; Qi-wei, Y. The structure and magnetic properties of $La_{2-2x}Sr_1Ca_{2x}Mn_2O_7$(x= 0.25-1.00). *Chin. Phys* **2001**, *10* (9), 857-861.

(5) Suryanarayanan, R.; Dhalenne, G.; Revcolevschi, A.; Prellier, W.; Renard, J. P.; Dupas, C.; Caliebe, W.; Chatterji, T. Colossal magnetoresistance and re-entrant charge ordering in single crystalline two layer Mn perovskite $LaSr_2Mn_2O_7$. *Solid State Commun.* **1999**, *113* (5), 267-271.

(6) Gupta, A. K.; Bhalla, G. L.; Khare, N. Magnetic phase diagram of double-layered $La_{2-2x}Ca_{1+2x}Mn_2O_7$ manganite. *J Phys Chem Solids* **2006**, *67* (11), 2358-2364.

(7) Fanah, S. J.; Ramezanipour, F. Lithium-Ion Mobility in Layered Oxide $Li_2(La_{0.75}Li_{0.25})(Ta_{1.5}Ti_{0.5})O_7$ Containing Lithium on both Intra and Inter-Stack Positions. *Eur. J. Inorg. Chem.* **2022**, *2022* (7), e202100950.

(8) Fanah, S. J.; Ramezanipour, F. Strategies for Enhancing Lithium-Ion Conductivity of Triple-Layered Ruddlesden–Popper Oxides: Case Study of $Li_{2-x}La_{2-y}Ti_{3-z}Nb_zO_{10}$. *Inorg. Chem.* **2020**, *59* (14), 9718-9727.

(9) Fanah, S. J.; Ramezanipour, F. Enhancing the lithium-ion conductivity in $Li_2SrTa_{2-x}Nb_xO_7$ (x = 0–2). *Solid State Sci.* **2019**, *97*, 106014.

(10) Zhu, Y.; Tahini, H. A.; Hu, Z.; Dai, J.; Chen, Y.; Sun, H.; Zhou, W.; Liu, M.; Smith, S. C.; Wang, H.; et al. Unusual synergistic effect in layered Ruddlesden−Popper oxide enables ultrafast hydrogen evolution. *Nat. Commun.* **2019**, *10* (1), 149.

(11) Yin, B.; Li, Y.; Sun, N.; Ji, X.; Huan, Y.; Dong, D.; Hu, X.; Wei, T. Activating ORR and OER in Ruddlesden-Popper based catalysts by enhancing interstitial oxygen and lattice oxygen redox reactions. *Electrochim. Acta* **2021**, *370*, 137747.

(12) Yatoo, M. A.; Du, Z.; Yang, Z.; Zhao, H.; Skinner, S. J. $La_xPr_{4-x}Ni_3O_{10-\delta}$: Mixed A-Site Cation Higher-Order Ruddlesden-Popper Phase Materials as Intermediate-Temperature Solid Oxide Fuel Cell Cathodes. *Crystals* **2020**, *10*, 428.

(13) Liang, Q.; Brocks, G.; Bieberle-Hütter, A. Oxygen evolution reaction (OER) mechanism under alkaline and acidic conditions. *J Phys: Energy* **2021**, *3* (2), 026001.

(14) Man, I.; Su, H.-Y.; Calle-Vallejo, F.; Hansen, H.; Hansen, A.; Nilay; Inoglu, G.; Kitchin, J.; Jaramillo, T.; Nørskov, J.; et al. Universality in Oxygen Evolution Electrocatalysis on Oxide Surfaces. *ChemCatChem* **2011**, *3*, 1159 –1165.

(15) Song, F.; Bai, L.; Moysiadou, A.; Lee, S.; Hu, C.; Liardet, L.; Hu, X. Transition Metal Oxides as Electrocatalysts for the Oxygen Evolution Reaction in Alkaline Solutions: An Application-Inspired Renaissance. *J. Am. Chem. Soc.* **2018**, *140* (25), 7748-7759.
(16) Hu, F.; Yu, D.; Ye, M.; Wang, H.; Hao, Y.; Wang, L.; Li, L.; Han, X.; Peng, S. Lattice-Matching Formed Mesoporous Transition Metal Oxide Heterostructures Advance Water Splitting by Active Fe–O–Cu Bridges. *Adv. Energy Mater.* **2022**, *12* (19), 2200067.
(17) Deng, L.; Hu, F.; Ma, M.; Huang, S.-C.; Xiong, Y.; Chen, H.-Y.; Li, L.; Peng, S. Electronic Modulation Caused by Interfacial Ni-O-M (M=Ru, Ir, Pd) Bonding for Accelerating Hydrogen Evolution Kinetics. *Angew. Chem. Int. Ed.* **2021**, *60* (41), 22276-22282.
(18) Hona, R. K.; Karki, S. B.; Ramezanipour, F. Oxide Electrocatalysts Based on Earth-Abundant Metals for Both Hydrogen- and Oxygen-Evolution Reactions. *ACS Sustain. Chem. Eng.* **2020**, *8* (31), 11549-11557.
(19) Hona, R. K.; Ramezanipour, F. Remarkable Oxygen-Evolution Activity of a Perovskite Oxide from the $Ca_{2-x}Sr_xFe_2O_{6-\delta}$ Series. *Angew. Chem.* **2019**, *131*, 2082-2085.
(20) Karki, S. B.; Ramezanipour, F. Pseudocapacitive Energy Storage and Electrocatalytic Hydrogen-Evolution Activity of Defect-Ordered Perovskites $Sr_xCa_{3-x}GaMn_2O_8$ (x = 0 and 1). *ACS Appl. Energy Mater.* **2020**, *3* (11), 10983-10992.
(21) Retuerto, M.; Pascual, L.; Calle-Vallejo, F.; Ferrer, P.; Gianolio, D.; Pereira, A. G.; García, Á.; Torrero, J.; Fernández-Díaz, M. T.; Bencok, P.; et al. Na-doped ruthenium perovskite electrocatalysts with improved oxygen evolution activity and durability in acidic media. *Nat. Commun* **2019**, *10* (1), 2041.
(22) Hona, R. K.; Karki, S. B.; Cao, T.; Mishra, R.; Sterbinsky, G. E.; Ramezanipour, F. Sustainable Oxide Electrocatalyst for Hydrogen- and Oxygen-Evolution Reactions. *ACS Catal.* **2021**, *11* (23), 14605-14614.
(23) Karki, S. B.; Andriotis, A. N.; Menon, M.; Ramezanipour, F. Bifunctional Water-Splitting Electrocatalysis Achieved by Defect Order in $LaA_2Fe_3O_8$ (A = Ca, Sr). *ACS Appl. Energy Mater.* **2021**, *4* (11), 12063-12066.
(24) Alom, M. S.; Ramezanipour, F. Layered Oxides $SrLaFe_{1-x}Co_xO_{4-\delta}$ (x=0–1) as Bifunctional Electrocatalysts for Water-Splitting. *ChemCatChem* **2021**, *13* (15), 3510-3516.
(25) Alom, M. S.; Kananke-Gamage, C. C. W.; Ramezanipour, F. Perovskite Oxides as Electrocatalysts for Hydrogen Evolution Reaction. *ACS Omega* **2022**, *7* (9), 7444-7451.
(26) Hona, R. K.; Ramezanipour, F. Effect of the Oxygen Vacancies and Structural Order on the Oxygen Evolution Activity: A Case Study of $SrMnO_{3-\delta}$ Featuring Four Different Structure Types. *Inorg. Chem.* **2020**, *59* (7), 4685-4692.
(27) Hona, R. K.; Ramezanipour, F. Structure-dependence of electrical conductivity and electrocatalytic properties of $Sr_2Mn_2O_6$ and $CaSrMn_2O_6$. *J Chem Sci* **2019**, *131* (11), 109.
(28) Karki, S. B.; Hona, R. K.; Yu, M.; Ramezanipour, F. Enhancement of Electrocatalytic Activity as a Function of Structural Order in Perovskite Oxides. *ACS Catal.* **2022**, 10333-10337.
(29) Kananke-Gamage, C. C. W.; Ramezanipour, F. Variation of the electrocatalytic activity of isostructural oxides $Sr2LaFeMnO_7$ and $Sr2LaCoMnO_7$ for hydrogen and oxygen-evolution reactions. *Dalton Trans.* **2021**, *50* (40), 14196-14206.
(30) Dai, J. M.; Yuan, G. Y.; Song, W. H.; Sun, Y. P. The behavior of photoinduced charge delocalization in bilayer manganite $LaCa_2Mn_2O_7$. *Physica B: Condensed Matter* **2006**, *371* (2), 245-248.
(31) Zhu, J. L.; Yu, R. C.; Li, F. Y.; Jin, C. Q.; Zhang, Z. The structure and properties of the manganate with nominal composition $La_{1.0}Ca_{2.0}Mn_2O_7$. *Mater. Sci. Eng., B* **2002**, *95* (1), 19-23.

(32) Gupta, A. K.; Kumar, V.; Khare, N. Hopping conduction in double layered $La_{2-2x}Ca_{1+2x}Mn_2O_7$ manganite. *Solid State Sci.* **2007**, *9* (9), 817-823.
(33) Ehsani, M. H.; Mehrabad, M. J.; Kameli, P.; Ghazi, M. E.; Razavi, F. S. Low-Temperature Electrical Resistivity of Bilayered $LaSr_2Mn_2O_7$ Manganite. *J. Low Temp. Phys* **2016**, *183*, 359-370.
(34) Ehsani, M.; Ghazi, M.; Kameli, P. Effects of pH and sintering temperature on the synthesis and electrical properties of the bilayered $LaSr_2Mn_2O_7$ manganite prepared by the sol-gel process. *J. Mater. Sci.* **2012**, *47*, 5815-5822.
(35) Nair, Mahesh M.; Abanades, S. Experimental screening of perovskite oxides as efficient redox materials for solar thermochemical CO_2 conversion. *Sustain. Energy Fuels* **2018**, *2* (4), 843-854.
(36) Li, Q.; Guo, M.; Wang, K.; Wei, Z.; Du, G.; Zhang, G.; Chen, N. $LaSr_2Mn_2O_7$ Ruddlesden-Popper manganites for oxygen reduction and electrochemical capacitors. *J. Rare Earths* **2020**, *38* (7), 763-769.
(37) Dreele, A. C. L. a. R. B. V. General Structure Analysis System (GSAS). *Los Alamos National Laboratory Report LAUR* **2004**, 86–748.
(38) Toby, B. H. EXPGUI, a graphical user interface for GSAS. *J. Appl. Crystallogr.* **2001**, *34*, 210-213.
(39) Hona, R. K.; Ramezanipour, F. Disparity in electrical and magnetic properties of isostructural oxygen-deficient perovskites $BaSrCo_2O_{6-\delta}$ and $BaSrCoFeO_{6-\delta}$. *J. Mater. Sci.: Mater. Electron.* **2018**, *29* (16), 13464-13473.
(40) Jeerage, K. M.; Candelaria, S. L.; Stavis, S. M. Rapid Synthesis and Correlative Measurements of Electrocatalytic Nickel/Iron Oxide Nanoparticles. *Sci. Rep.* **2018**, *8*, 4584.
(41) Du, X.; Ma, G.; Zhang, X. Experimental and Theoretical Understanding on Electrochemical Activation Processes of Nickel Selenide for Excellent Water-Splitting Performance: Comparing the Electrochemical Performances with M–NiSe (M = Co, Cu, and V). *ACS Sustain. Chem. Eng.* **2019**, *7*, 19257-19267.
(42) Du, X.; Su, H.; Zhang, X. Metal–Organic Framework-Derived Cu-Doped Co_9S_8 Nanorod Array with Less Low-Valence Co Sites as Highly Efficient Bifunctional Electrodes for Overall Water Splitting. *ACS Sustainable Chem. Eng.* **2019**, *7*, 16917-16926.
(43) Shannon, R. D. Revised effective ionic radii and systematic studies of interatomic distances in halides and chalcogenides. *Acta Crystallogr., Sect. A* **1976**, *32* (5), 751-767.
(44) Green, M. A.; Neumann, D. A. Synthesis, Structure, and Electronic Properties of $LaCa_2Mn_2O_7$. *Chem. Mater.* **2000**, *12*, 90-97.
(45) Wudl, F.; Bryce, M. R. Apparatus for two-probe conductivity measurements on compressed powders. *J. Chem. Educ.* **1990**, *67* (8), 717.
(46) Hona, R. K.; Huq, A.; Mulmi, S.; Ramezanipour, F. Transformation of Structure, Electrical Conductivity, and Magnetism in $AA'Fe_2O_{6-\delta}$, A = Sr, Ca and A′ = Sr. *Inorg. Chem.* **2017**, *56* (16), 9716-9724.
(47) Karki, S. B.; Ramezanipour, F. Magnetic and electrical properties of $BaSrMMoO_6$ (M = Mn, Fe, Co, and Ni). *Mater. Today Chem.* **2019**, *13*, 25-33.
(48) Ehsani, M. H.; Ghazi, M. E.; Kameli, P.; Razavi, F. S. DC magnetization studies of nano- and micro-particles of bilayered manganite $LaSr_2Mn_2O_7$. *J. Alloys Compd.* **2014**, *586*, 261-266.
(49) Wang, H.; Zhou, H.; Zhang, W.; Yao, S. Urea-assisted synthesis of amorphous molybdenum sulfide on P-doped carbon nanotubes for enhanced hydrogen evolution. *J. Mater. Sci.* **2018**, *53* (12), 8951-8962.

(50) Gong, Q.; Wang, Y.; Hu, Q.; Zhou, J.; Feng, R.; Duchesne, P. N.; Zhang, P.; Chen, F.; Han, N.; Li, Y.; et al. Ultrasmall and phase-pure W_2C nanoparticles for efficient electrocatalytic and photoelectrochemical hydrogen evolution. *Nat. Commun* **2016**, *7* (1), 13216.
(51) Li, Y. H.; Liu, P. F.; Pan, L. F.; Wang, H. F.; Yang, Z. Z.; Zheng, L. R.; Hu, P.; Zhao, H. J.; Gu, L.; Yang, H. G. Local atomic structure modulations activate metal oxide as electrocatalyst for hydrogen evolution in acidic water. *Nat. Commun* **2015**, *6* (1), 8064.
(52) Feng, H.; Xu, Z.; Ren, L.; Liu, C.; Zhuang, J.; Hu, Z.; Xu, X.; Chen, J.; Wang, J.; Hao, W.; et al. Activating Titania for Efficient Electrocatalysis by Vacancy Engineering. *ACS Catal.* **2018**, *8* (5), 4288-4293.
(53) Morales, D. M.; Risch, M. Seven steps to reliable cyclic voltammetry measurements for the determination of double layer capacitance. *JPhys Energy* **2021**, *3* (3), 034013.
(54) Hona, R. K.; Ramezanipour, F. Effect of the Oxygen Vacancies and Structural Order on the Oxygen Evolution Activity: A Case Study of $SrMnO_{3-\delta}$ Featuring Four Different Structure Types. *Inorg. Chem.* **2020**, *59*, 4685-4692.
(55) Zhu, Y.; Zhou, W.; Sunarso, J.; Zhong, Y.; Shao, Z. Phosphorus-Doped Perovskite Oxide as Highly Efficient Water Oxidation Electrocatalyst in Alkaline Solution. *Adv. Funct. Mater.* **2016**, *26* (32), 5862-5872.
(56) Lasia, A. Mechanism and kinetics of the hydrogen evolution reaction. *Int. J. Hydrog. Energy* **2019**, *44* (36), 19484-19518.
(57) Chen, G.-F.; Ma, T. Y.; Liu, Z.-Q.; Li, N.; Su, Y.-Z.; Davey, K.; Qiao, S.-Z. Efficient and Stable Bifunctional Electrocatalysts Ni/Ni_xM_y (M = P, S) for Overall Water Splitting. *Adv. Funct. Mater.* **2016**, *26* (19), 3314-3323.